Pergamon

Int. J. Heat Mass Transfer. Vol. 41, No. 12, pp. 1655–1666, 1998

Printed in Great Britain
0017–9310/98 $19.00 + 0.00

PII: S0017–9310(97)00285–8

Direct simulation of vapor bubble growth

SAMUEL W. J. WELCH†

Department of Mechanical Engineering, University of Colorado at Denver, Denver, Colorado, U.S.A.

(*Received* 9 *January* 1997 *and in final form* 17 *September* 1997)

Abstract—This paper presents a numerical method directed towards the local simulation of axisymmetric vapor bubble growth. We use an interface tracking method in conjunction with a finite volume method on a moving unstructured mesh. We allow metastable bulk states and assume the interface exists in thermal and chemical equilibrium. The bulk fluids are viscous, conducting, and compressible. The control volume continuity, momentum and energy equations are modified in the presence of a phase interface to include surface tension and discontinuous pressure and velocity. A solid wall model is included to allow for conjugate heat transfer modes. © 1998 Elsevier Science Ltd. All rights reserved.

1. INTRODUCTION

Heterogeneous nucleate boiling is a fundamental process important in engineering thermal fluid mechanics. The continual wetting and rewetting of the heated surface by the liquid phase along with the efficient heat transfer promoted by the use of the latent heat of vaporization makes nucleate boiling a preferred mode of heat transfer in heat exchanging equipment. This importance has led to decades of experimental and theoretical studies. Early research focused on understanding the problem of homogeneous vapor bubble growth. Plesset and Zwick [1] took advantage of the spherical symmetry inherent in homogeneous nucleate boiling to provide an analytical solution for diffusion controlled vapor bubble growth. This solution used a lumped parameter model for the vapor phase, included surface tension and took into consideration the thin thermal layer on the liquid side of the phase interface. Mikic *et al.* [2] used a matched asymptotic expansion to match the inertial controlled early growth solution to the above mentioned diffusion controlled solution. This solution was extended to the heterogeneous case by the use of a shape factor. Workers found difficulty matching analytic solutions of this type to experimental data. The currently accepted explanations for this discrepancy are that heterogeneous bubble growth is enhanced by either a microconvection mechanism or a liquid microlayer at the base of the bubble [3, 4].

There is a growing body of literature in which workers have successfully matched experimental data to models of heterogeneous bubble growth by including a microlayer in their model. Wang and Bankoff [5] included the microlayer surface area in their model of bubble growth in a depressurizing liquid. The results were in good agreement with their experimental data. Mei *et al.* [6, 7] consider the conduction of heat from a solid through a liquid microlayer to the liquid–vapor interface in a model for saturated boiling. They successfully match experimental data with this approach. It is worth noting that their model required the use of two parameters obtained from experimental data on the microlayer and bubble shapes. A similar model was used by Guo and El-Genk [8] in their analysis of vapor bubble growth on a composite solid. An outstanding feature in the work of Mei *et al.* and of Guo and El-Genk is that the thermal field in the solid is shown to be of importance in heterogeneous vapor bubble growth.

Despite this progress there are still fundamental aspects of nucleate boiling that are not well understood. The models discussed above do not solve for the hydrodynamics of the fluid flow, nor do they locate the moving phase interface. This information is included through the use of correlations making use of experimental data. There is interest in solving the moving boundary hydrodynamics problem to increase the understanding of the various mechanisms in heterogeneous bubble growth. For example, bubble departure models usually make assumptions about the comparative magnitudes of buoyancy forces, surface tension forces, inertial forces and viscous drag forces [9, 10]. The experimental data for bubble departure diameters shows considerable scatter when compared to many of the correlations [9]. These correlations generally assume one or more of the above mentioned forces is either dominant or negligible. Verification of these assumptions would be of considerable interest in improving these types of correlations. One approach to verifying these assumptions and improving our understanding of the basic mechanisms of nucleate boiling is through numerical simulation. This

† Mechanical Engineering Department, University of Colorado at Denver, P.O. Box 173364, Campus Box 112, Denver, Colorado 80217, U.S.A. Tel.: (303) 556-8516. E-mail: sam@carbon.cudenver.edu.

NOMENCLATURE

$A(t)$	time dependent area with normal in azimuthal direction
A, B	constants in bubble growth equation from Mikic *et al.* [8]
$C(t)$	time dependent curve describing intersection of phase interface with $S(t)$
C_{pl}, C_s	liquid specific heat, solid specific heat
e	fluid internal energy
g	Gibb's potential
h_{lg}	latent heat of vaporization
$\hat{\mathbf{i}}$, $\hat{\mathbf{j}}$	unit vector in x-direction (radial direction for $\theta = 0$) and y-direction
Ja	Jakob number
$\mathbf{n}$	outward directed unit normal vector
P	pressure
$\mathbf{q}$	heat flux vector, Fourier's law assumed
r, $\bar{r}$	radial coordinate, average radial coordinate on area $A(t)$
R^+	non-dimensional bubble radius
$S(t)$	surface area of moving control volume (t)
t	time
T^v	viscous stress tensor
$\mathbf{v}$, $\mathbf{v}_s$	fluid velocity, mesh and interfacial velocity
$V(t)$	time dependent control volume
x, y	Cartesian coordinates.

Greek symbols

α_l	liquid diffusivity
γ	surface tension
θ	azimuthal coordinate in cylindrical coordinate system
ϑ, ϑ_{sat}	temperature, saturation temperature
μ, ρ	fluid viscosity, density
ρ_s	solid density
$\boldsymbol{\tau}$	unit tangent vector
Ψ	general conserved variable.

Subscripts

g, l	vapor and liquid phases, respectively
0	reference state.

paper presents a correlation free numerical approach suitable for the local simulation of vapor bubble growth. The important feature of the method presented is that the interface between the liquid and vapor phases is tracked in flows with mass transfer. We feel that this approach will eventually enable us to simulate heterogeneous bubble growth including hydrodynamics and the evolution of the bubble shape along with the formation of the liquid microlayer.

During the last decade, numerical approaches to address this problem have begun to appear in the literature. Lee and Nydahl [11] used an assumed bubble and microlayer shape to simulate the growth and departure of vapor bubbles. Their method used a lumped parameter model for the vapor phase and required an empirical relationship to complete the geometry. Results of their work were used in the experimental work of Zeng *et al.* [10] to aid in the development of a more accurate bubble departure model. A similar numerical approach was taken by Patil and Prusa [12] who assumed a hemispherical shape in simulating vapor bubble growth on a heated wall. In these methods, the bubble shape is assumed. In order to simulate bubble growth including the evolution of the bubble shape, hence eliminating the need for correlations, it is necessary to include interface tracking capability.

The problem of vapor bubble growth poses special difficulties for interface tracking methods. The major difficulty is that the liquid and vapor velocities are discontinuous across the phase interface. An additional difficulty is that there typically exists a thermal layer which moves with the phase interface. The Volume of Fluid (VOF) advection and reconstruction algorithms [13] assume a continuous velocity field as does the interface tracking method in the paper by Tryggvason [14]. The Level Set Method of Osher and Sethian has been applied to problems in which the interface is not simply advected with the fluid [15], but the method has not been applied to problems of liquid–vapor phase change. These methods are implemented on Eulerian grids and are able to track interfaces in fluid flows in which there is significant interfacial distortion and change in topology. VOF methods have been used in conjunction with two-fluid models [16] and the homogeneous equilibrium model [17] for calculations of flows involving liquid–vapor phase change. These methods, while useful in industrial simulations, are not intended to capture local physics near phase interfaces and require the use of correlations or the assumption of homogeneous equilibrium to complete the problem formulation. The method presented in this work is more closely related to Lagrangian methods. Typically, Lagrangian methods are able to capture interfacial physics with higher fidelity than Eulerian methods, but are unable to follow the overall interfacial motions that Eulerian methods are capable of following.

An additional difficulty in simulating bubble growth is that the interface tracking method must accurately calculate gradients near the moving interface. Consider a simplified form of the energy jump condition at a phase interface:

$$\dot{m}h_{lg} = \|\mathbf{q}\| \cdot \mathbf{n}. \tag{1}$$

This relationship indicates that the mass transfer rate and hence the interfacial motion is determined largely by the temperature gradient near the phase interface. For vapor bubble growth, this gradient exists in a thin layer on the liquid side of the interface. In addition, this relationship indicates that if the liquid is in a metastable state, the thermal layer tends to be sucked into the phase interface. As the interface moves, it is essential that the grid structure has high resolution near the interface. This is an additional difficulty for Eulerian methods as this may require high grid resolution in regions where it is not necessary.

The difficulties in applying existing interface tracking techniques to liquid–vapor phase change problems led us to develop a two-dimensional method directed to problems of this type [18]. In our method, the interface is embedded within control volumes defined on a moving triangular mesh. The interface is tracked with nodes affixed on the liquid and vapor sides at the same spatial location. The moving mesh allows us to keep a high grid resolution near the interface in order to accurately represent the steep gradients attendant with the mass transfer problem. There is a discontinuity of the normal component of the fluid velocity and pressure across the moving phase interface. We solve finite volume mass, momentum and energy equations for both the liquid and vapor phases. Both phases are viscous, conducting and compressible fluids. The state equations are extended smoothly into the saturation region allowing for the existence of metastable states. At the phase interface, we assume thermodynamic equilibrium. The interfacial motion is found from the physics while the mesh motion in the bulk regions is calculated by simple interpolation with neighboring nodes. In this paper, we extend this method to axisymmetric flows and we add a solid, conducting wall in order to simulate heterogeneous vapor bubble growth.

The outline for this paper is as follows. We state the governing equations in Section 2 and discuss the numerical method in Section 3. Simulations are presented in Section 4.

2. THE BASIC EQUATIONS

For our method we must express the basic equations in integral form for non-material, moving volumes with embedded phase interfaces. Such a volume is shown in Fig. 1. Neglecting surface properties other than surface tension, the continuity, momentum, and total energy equations for these volumes may be expressed as

$$\frac{\mathrm{d}}{\mathrm{d}t}\int_{V(t)}\rho\,\mathrm{d}V+\int_{S(t)}\rho(\mathbf{v}-\mathbf{v}_s)\cdot\mathbf{n}\,\mathrm{d}S=0 \tag{2}$$

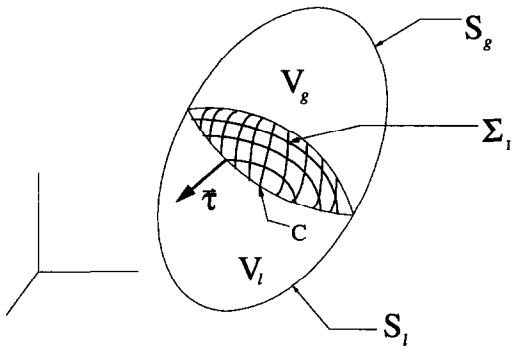

Fig. 1. Non-material, moving volume with embedded phase interface.

$$\frac{\mathrm{d}}{\mathrm{d}t}\int_{V(t)}\rho\mathbf{v}\,\mathrm{d}V+\int_{S(t)}\rho\mathbf{v}(\mathbf{v}-\mathbf{v}_s)\cdot\mathbf{n}\,\mathrm{d}S$$
$$=-\int_{S(t)}P\mathbf{n}\,\mathrm{d}S+\int_{S(t)}T^{v}\cdot\mathbf{n}\,\mathrm{d}S+\int_{V(t)}\rho\mathbf{b}\,\mathrm{d}V$$
$$+\int_{C(t)}\gamma\boldsymbol{\tau}\,\mathrm{d}C \tag{3}$$

$$\frac{\mathrm{d}}{\mathrm{d}t}\int_{V(t)}\rho\left(e+\frac{1}{2}\mathbf{v}\cdot\mathbf{v}\right)\mathrm{d}V$$
$$+\int_{S(t)}\rho\left(e+\frac{1}{2}\mathbf{v}\cdot\mathbf{v}\right)(\mathbf{v}-\mathbf{v}_s)\cdot\mathbf{n}\,\mathrm{d}S$$
$$=\int_{C(t)}\gamma\mathbf{v}\cdot\boldsymbol{\tau}\,\mathrm{d}C-\int_{S(t)}P\mathbf{v}\cdot\mathbf{n}\,\mathrm{d}S$$
$$+\int_{S(t)}\mathbf{v}\cdot T^{v}\cdot\mathbf{n}\,\mathrm{d}S+\int_{V(t)}\rho\mathbf{v}\cdot\mathbf{b}\,\mathrm{d}V-\int_{S(t)}\mathbf{q}\cdot\mathbf{n}\,\mathrm{d}S \tag{4}$$

where $\boldsymbol{\tau}$ is a unit vector in the tangent plane of the interface outwardly directed from the volume $V(t)$. Here $V(t)=V_l\cup V_g$, $S(t)=S_l\cup S_g$ and Σ_I is the phase interface. $C(t)$ is a curve describing the intersection of the interface with the surface $S(t)$. We note that single phase regions are described by similar equations with no surface tension terms where $V(t)$ and $S(t)$ are the single phase control volume and surface, respectively. We use the total energy equation as it is a conservative form. With this set of basic equations we must include the kinematic relationship between the mesh motion and the time rate of change of the control volume

$$\frac{\mathrm{d}}{\mathrm{d}t}\int_{V(t)}\mathrm{d}V-\int_{S(t)}\mathbf{v}_s\cdot\mathbf{n}\,\mathrm{d}S=0. \tag{5}$$

We used linearized state equations for internal energy and density with temperature and pressure as the independent variables.

$$e = e(\vartheta, P) = e_0 + \left.\frac{\partial e}{\partial \vartheta}\right|_P (\vartheta - \vartheta_0) + \left.\frac{\partial e}{\partial P}\right|_\vartheta (P - P_0)$$

$$\rho = \rho(\vartheta, P) = \rho_0 + \left.\frac{\partial \rho}{\partial \vartheta}\right|_P (\vartheta - \vartheta_0) + \left.\frac{\partial \rho}{\partial P}\right|_\vartheta (P - P_0) \quad (6)$$

a temperature dependent surface tension

$$\gamma = \gamma_0 + \frac{\partial \gamma}{\partial \vartheta}(\vartheta - \vartheta_0) \quad (7)$$

and the interface thermal equilibrium conditions.

$$\vartheta_g = \vartheta_l$$

$$g_g(P_g, \vartheta_g) = g_l(P_l, \vartheta_l). \quad (8)$$

Note that these interface conditions neglect the irreversibilities associated with heat and mass transfer at the interface. Generalization of these conditions to consider irreversible effects may be found in references [19] and [20]. At the interface we also enforce continuity of the tangential component of two phasic velocities

$$(\mathbf{v} \cdot \boldsymbol{\tau})_g = (\mathbf{v} \cdot \boldsymbol{\tau})_l. \quad (9)$$

3. THE NUMERICAL METHOD

In this section we describe the extension of the two dimensional interface tracking method presented in [18] to axisymmetric flows with a solid wall model. This method may be characterized as a conservative, low order, semi-implicit finite volume method on an unstructured, moving grid. Discrete approximations to the integrals comprising the control volume are arrived at by assuming linear shape functions on triangles and accumulating the contributions of each triangle in the control volume balance equations. Despite the fact that the spatial discretizations in our method are centered differences on a uniform grid, the spatial order is not claimed to be second order as our grids are not uniform. Formally, the spatial order is first order, but we obtain results closer to second order as will be demonstrated. The temporal discretization used is implicit except in the coefficients of the relative velocity in the flux terms, the body force terms, the viscous work terms, and the geometry used in forming the equations [18]. The time discretization may be characterized as a simple forward time method. Time step limitations are a convective limit and a capillary limit associated with the use of explicit geometry on the surface tension terms.

Control volumes containing phase interfaces must include the interfacial thermal and chemical equilibrium conditions along with surface tension force and work terms. Surface tension forces are added as vector forces acting on the boundary of the control volume. This treatment allows us to avoid calculation of the curvature and has been demonstrated in [18] to be accurate in simulations in which surface tension plays a dominant role. The interface conditions expressing thermal and chemical equilibrium are applied to the nodes representing the liquid and vapor phases at the same spatial location on the interface. The interfacial motion in the direction normal to the interface is determined by physics and must be determined as part of the solution procedure. The interfacial motion in the direction tangent to the interface is not determined by physics and is prescribed in such a way as to keep interfacial nodes equidistant from other interfacial nodes. The bulk mesh motion is not determined by physics and the simulations in this paper use simple implicit averaging with neighboring nodes to determine the bulk mesh motion. The method is closed by the implementation of two numerical boundary conditions at the interface. In the simulations presented in this paper we use simple linear pressure extrapolations on each side of the phase interface as the numerical boundary conditions. We believe that the moving boundary problem associated with phase interfaces across which there is mass transfer still contain some open questions of physics. The interested reader should consult the paper by Dell'Isola and Romano [21] in which the authors were forced to postulate an additional constitutive equation in their discussion. Another paper of interest is the paper by Huang and Joseph [22] in which the authors compare two sets of conditions at the phase interface in a stability problem.

In what follows, we discuss the extension of the two-dimensional spatial discretization [18] to the axisymmetric case. Consider the grid structure of Fig. 2 showing a few triangular elements in the r–z plane. In this plane, the control volume intersects the shaded area A. The control volume edges are defined as straight line segments from the area centroid of the triangles to the mid-points of the sides of the triangles. The control volume in Fig. 2 also contains an embedded phase interface lying on the edges of triangular elements. As is shown in Fig. 2, the control volume is created by rotating the area A about the z-axis from $-\Delta\theta/2$ to $\Delta\theta/2$. In order to obtain the axisymmetric approximation with a two dimensional code, we take the limit as $\Delta\theta \to 0$. In our discretizations we must evaluate surface integrals on the lateral surfaces, Σ, and azimuthal surfaces, A. We must also evaluate volume integrals over V and, if the control volume contains an embedded phase interface, line integrals along the curve $C(t)$.

3.1. *Volume integrals*

The time derivatives are evaluated by lumping the conserved variable, Ψ, at the node

$$\frac{\mathrm{d}}{\mathrm{d}t}\int_{V(t)} \Psi \,\mathrm{d}V \cong \frac{\mathrm{d}}{\mathrm{d}t}(\Psi V) = \Psi \frac{\mathrm{d}V}{\mathrm{d}t} + V \frac{\mathrm{d}\Psi}{\mathrm{d}t} \quad (10)$$

where $V = \bar{r}(\Delta\theta)A(t)$ with $\bar{r}$ with the radial coordinate of the area center for the control volume in the r–z plane. The body force terms in momentum and energy are lumped in a similar manner.

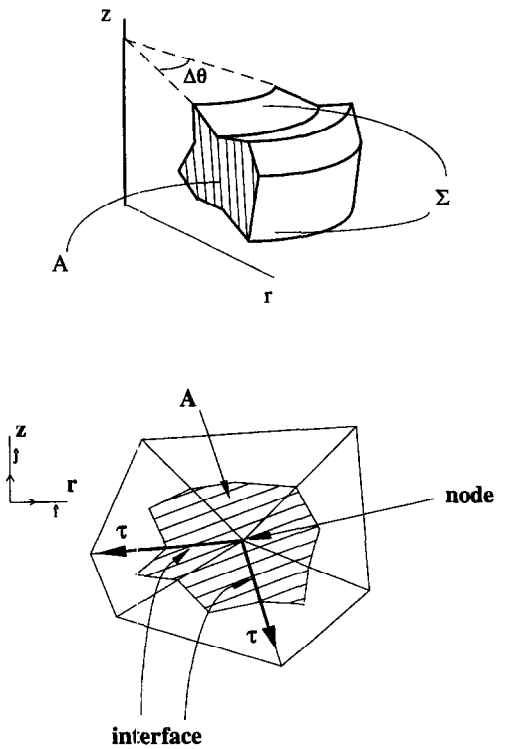

Fig. 2. Top: Three dimensional view of a control volume showing azimuthal surface (A) and lateral surface (Σ). Bottom: Two dimensional discretized control volume (shaded area) with embedded phase interface on a triangular mesh.

3.2. *Azimuthal surface integrals*

Due to the axisymmetry, there is no mass flux across the azimuthal surfaces and we need only calculate pressure and normal stress forces on these surfaces. On these surfaces the outward directed normal, $\mathbf{n}$, does not vary. Furthermore, due to the axisymmetry, the pressure forces and normal stress forces on the front and back faces cancel in the azimuthal direction. The momentum pressure surface integral becomes

$$\int_{A(t)} P\mathbf{n}\,\mathrm{d}A = -\hat{\mathbf{i}}(\Delta\theta)\int_{A(t)} P\,\mathrm{d}A \qquad (11)$$

where $\hat{\mathbf{i}}$ is a unit vector in the cartesian x-direction. The pressure varies linearly over the separate regions making up the area A (shown in Fig. 2) and this integral is evaluated exactly using these linear profiles. The momentum viscous stress surface integral is evaluated in a similar manner. The pressure and velocity in these terms are treated implicitly.

3.3. *Lateral surface integrals*

Integrals over the lateral surfaces comprise the majority of the surface integrals that need be evaluated. There is pressure force and pressure work along with viscous forces and viscous work on these surfaces. There is also mass flux across these surfaces along with volume changes associated with the motion of these surfaces. These integrations can be approximated by forming the surface element, $r\,\mathrm{d}\theta\,\mathrm{d}l$ and integrating out the θ dependence (only the unit normal, $\mathbf{n}$, is a function of θ). Here, l is the length of the edge of the surface in the r–z plane. The results can be expressed as one of the following forms:

$$\int_{\Sigma(t)} \Phi\mathbf{n}\,\mathrm{d}S = (n_x\hat{\mathbf{i}}+n_j\hat{\mathbf{j}})(\Delta\theta)\int_0^l \Phi r\,\mathrm{d}l \qquad (12)$$

$$\int_{\Sigma(t)} \boldsymbol{\Phi}\cdot\mathbf{n}\,\mathrm{d}S = (n_x\hat{\mathbf{i}}+n_j\hat{\mathbf{j}})(\Delta\theta)\cdot\int_0^l \boldsymbol{\Phi} r\,\mathrm{d}l \qquad (13)$$

where Φ may be a scalar or vector field. Along the straight line segments Φ and r vary linearly along the length l and the integrals are evaluated exactly. Further details of the lateral surface discretization may be found in [18].

3.4. *Line integral over* C(t) *and control volumes containing phase interfaces*

For control volumes containing phase interfaces, the closed curve $C(t)$ appears on surfaces of both types. As with the surface integrals on azimuthal surfaces, symmetry considerations lead to the following contribution to the line integral across the azimuthal surfaces

$$\int_{C_A(t)} \gamma\boldsymbol{\tau}\,\mathrm{d}C = -\hat{\mathbf{i}}(\Delta\theta)\int_{C_A(t)} \gamma\,\mathrm{d}C. \qquad (14)$$

The surface tension is a linear function of temperature, hence this integration is a simple application of the trapezoidal rule. On lateral surfaces, the contribution to the line integral is

$$\int_{C_\Sigma(t)} \gamma\boldsymbol{\tau}\,\mathrm{d}C = (n_x\hat{\mathbf{i}}+n_j\hat{\mathbf{j}})(\Delta\theta)r\gamma. \qquad (15)$$

The total line integration is the sum of the line integrals over all line segments. The line integrals are added to the momentum and energy control volume equations for control volumes containing phase interfaces. The volume conservation equation, equation (5), is applied to the liquid and vapor phases separately [see equation (10)]. Therefore, the discrete control volume equations containing phase interfaces must also contain the term [18]

$$[\Psi_l-\Psi_g]\int_{\Sigma_I(t)} \mathbf{v}_s\cdot\mathbf{n}\,\mathrm{d}S. \qquad (16)$$

Here $\Sigma_I(t)$ is the interfacial surface separating the phases in the control volume.

3.5. *Control volumes containing a solid*

We write an energy balance for the control volumes containing a solid simply by summing the energy balances for the liquid region and the energy balance for the solid region. Note that the flux terms across the surface defining the solid wall will cancel in this operation. The resulting control volume energy balance is:

$$\frac{\mathrm{d}}{\mathrm{d}t}\int_{V(t)}\rho\left(e+\frac{1}{2}\mathbf{v}\cdot\mathbf{v}\right)\mathrm{d}V + \int_{S(t)}\rho\left(e+\frac{1}{2}\mathbf{v}\cdot\mathbf{v}\right)(\mathbf{v}-\mathbf{v}_s)\cdot\mathbf{n}\,\mathrm{d}S + \frac{\mathrm{d}}{\mathrm{d}t}\int_{V_s}\rho_s C_s(\vartheta-\vartheta_0)\,\mathrm{d}V = -\int_{S(t)}P\mathbf{v}\cdot\mathbf{n}\,\mathrm{d}S + \int_{S(t)}\mathbf{v}\cdot T^{v}\cdot\mathbf{n}\,\mathrm{d}S + \int_{V(t)}\rho\mathbf{v}\cdot\mathbf{b}\,\mathrm{d}V - \int_{S(t)}\mathbf{q}\cdot\mathbf{n}\,\mathrm{d}S - \int_{S_s}\mathbf{q}\cdot\mathbf{n}\,\mathrm{d}S. \quad (17)$$

Here, $V(t)$ and $S(t)$ refer to the time varying volume and surface of the liquid region, respectively. V_s and S_s refer to the stationary volume and surface of the solid region, respectively. The spatial and temporal discretizations formed for this equation are identical to those used for the fluid region. The lone exception is the integral over S_s which is treated explicitly. Control volumes containing only a solid are a special case of the above equation with integrals over only V_s and S_s. We note that implicit in this formulation is that the solid nodes are stationary. It is a simple extension to move solid nodes but this extension is unnecessary for the simulations presented in this work.

3.6. *The overall system of equations*

Inspection of the spatial discretizations given above indicates that $\Delta\theta$ factors out of all of the terms in the continuity, momentum, and energy equations. These discrete approximations, along with the algebraic equations representing the interfacial conditions for interfacial nodes, make up a set of linear equations in the unknowns. The unknowns are the fluid velocity, the mesh velocity, the pressure and temperature at each node. These linear equations are assembled into a large, sparse, unsymmetric linear system of equations. This system of equations may be solved by any technique suitable for the solution of sparse non-symmetric systems. We currently use an ILU preconditioned transpose free quasi minimum residual method [23].

4. SAMPLE SIMULATIONS

In this section we present various simulations depicting vapor bubble growth. The fluid in these simulations is water and the partial derivatives in the linearized state equations are obtained at the initial liquid pressure and corresponding saturation temperature. Initial conditions are found by specifying the initial liquid pressure, P_l, and satisfying the equilibrium conditions:

$$\vartheta_g = \vartheta_l$$
$$g_g(P_g,\vartheta_g) = g_l(P_l,\vartheta_l)$$
$$P_g - P_l = \frac{\gamma}{2R}. \quad (18)$$

Note that in the absence of dynamic flow conditions the control volume momentum equations reduce, in the normal direction, to the third of these equilibrium conditions.

4.1. *Homogeneous bubble growth*

We first present simulations of homogeneous bubble growth in a superheated liquid. Despite the spherical symmetry inherent in the physics, this simulation is a crucial test of numerical methods for liquid–vapor phase transitions. The ability to simulate homogeneous bubble growth indicates the ability to handle the discontinuous phase velocities as well as the ability to capture and follow the thermal layer as it moves with the phase interface. The accuracy of the numerical results is verified by comparison to the analytic solution of Mikic *et al.* [2], known to reasonably represent homogeneous bubble growth data:

$$R^+ = \tfrac{2}{3}[(t^+ + 1)^{3/2} - (t^+)^{3/2} - 1] \quad (19)$$

where

$$R^+ = \frac{RA}{B^2}, \quad t^+ = \frac{tA^2}{B^2} \quad (22)$$

and

$$A = \left\{\frac{2[\vartheta_0 - \vartheta_{sat}(P_0)]h_{lg}\rho_g}{\rho_l\vartheta_{sat}(P_0)}\right\}^{1/2}, \quad B = \left(\frac{12\alpha_l}{\pi}\right)^{1/2} Ja$$
$$Ja = \frac{[\vartheta_0 - \vartheta_{sat}(P_0)]C_{pl}\rho_l}{\rho_g h_{lg}}. \quad (23)$$

Shown in Fig. 3 is the computational grid used in

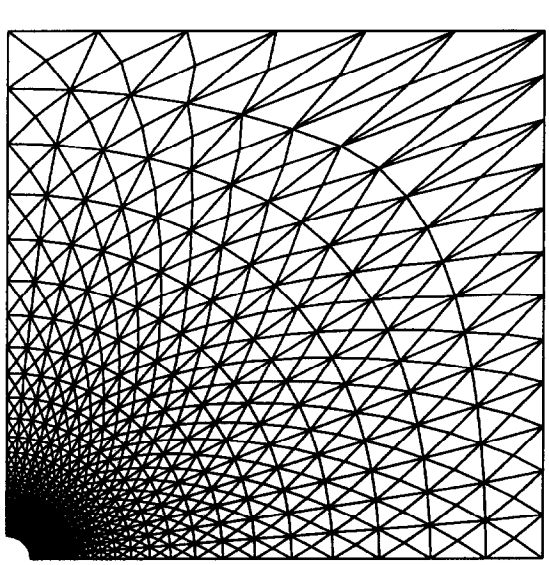

Fig. 3. Computational grid for homogeneous bubble growth simulations (vapor elements not shown for clarity). 612 vapor nodes, 870 liquid nodes, 19 interfacial nodes, 1482 total nodes.

Table 1. Bubble radius ($Ja = 15.7$) using three different time increments. Spatial grid shown in Fig. 4

	Time step	Cycle	Bubble radius
Coarse step	2.0×10^{-6} s	3100	0.9832 mm
Medium step	1.0×10^{-6} s	6200	0.9835 mm
Fine step	5.0×10^{-7} s	12400	0.9837 mm

Table 2. Bubble radius ($Ja = 15.17$) using three different spatial resolutions. Time increment = 1.0×10^{-6} s

	Cycle	Bubble radius
Coarse grid	6200	0.9905 mm
Medium grid	6200	0.9835 mm
Fine grid	6200	0.9827 mm

the following set of simulations. The left and bottom boundaries are treated as symmetry boundaries while the top and right boundaries are open boundaries. The original bubble shape is spherical with a radius of 0.1 mm (note that the analytic solution assumes zero initial radius). The initial conditions are those mentioned above with the liquid superheated by the amount $\Delta\vartheta$. Figure 4 shows comparisons of the bubble radius predicted by these simulations and the bubble radius predicted by the analytic solution. Once the initial transients die out, the results of the simulations are in reasonable agreement with the analytic solution for the Jakob numbers shown. Use of the linearized state equations limits us to Jakob in the range of these simulations.

We next consider the convergence properties of the method by first varying the time increment followed by varying the spatial resolution. The stability limit for these simulations is the capillary limit mentioned earlier (an approximate capillary limit may be found by restricting the shortest wavelength capillary wave to move no more than a grid spacing along the interface per time step). Table 1 shows results for a time convergence study in which the largest time step is near the approximate capillary limit. Table 2 shows results for a spatial convergence study with three successive grid resolution increases by a factor of 3/2. The medium spatial resolution is that shown in Fig. 2. The curves in Fig. 4 correspond to the medium spatial and temporal grid resolutions in Tables 1 and 2. These results indicate that the curve in Fig. 4 at $Ja = 15.17$ represents a nearly converged result.

4.2. *Heterogeneous bubble growth*

The simulations of heterogeneous bubble growth presented here are intended to illustrate the basic capability of the method. Future efforts will focus on improvements necessary to simulate the full ebullition cycle of heterogeneous bubble growth including microlayer growth and contact line physics. The liquid microlayer poses difficulties in that the computational grid can become severely distorted as the microlayer forms. Presently, our discrete convective operators are not fully implicit and the distorted grid causes difficulty due to the convective stability limit. The simulations presented in this work, therefore, do not include the full evolution of the microlayer. We note that Lee and Nydahl [11] did include a microlayer in their simulation using assumed geometry. We do not use an assumed microlayer geometry as initial conditions for pedagogical reasons as one of the motivations for developing our method is to simulate the formation of the liquid microlayer. To this end our current efforts are directed towards making the discrete convective operators fully implicit and improving our mesh motion algorithm.

In these simulations we consider the interface to be pinned at the contact line with the contact angle changing in time. Thus, the two phases as well as the interface are satisfying the no-slip condition. It is a simple matter to keep the contact angle constant and allow the interface to slide along the wall as is the case for a real system. We do not do so here as the contact line generally exists under a microlayer thus simulations including real contact line behavior must include the microlayer. The simulations in this work are intended to show the ability to track the interface in situations without spherical symmetry and in the presence of a conducting solid wall.

We begin our simulations by considering a vapor bubble on a wall, immersed in a superheated liquid. These conditions would arise when the surrounding liquid, initially at equilibrium with the vapor bubble, is depressurized thus creating a metastable liquid state. We consider water in equilibrium with it's vapor at a pressure of 0.1 Mpa. The metastable liquid state is created by raising the water temperature by two degrees Kelvin corresponding to a Jakob number of 6.1. The simulations include a steel wall with an adiabatic outer boundary. Shown in Fig. 5 is the geometry and a computational grid used in the simulations. We first use this problem to illustrate the convergence properties of the method for a problem without spherical symmetry. We use three grids with the element size increasing by a factor of 3/2. Table 3 shows the location of the bubble cap and the liquid, vapor and interface velocities at the cap for the three grid resolutions at the five hundredth time cycle (these simulations use a time step of 0.002 msec). The grid shown in Fig. 5 is the medium resolution grid referred to in Table 3. The low resolution grid has 16 interfacial elements (17 nodes), the medium resolution grid has 24 interface elements and the high resolution grid has 32 interface elements. Figure 6 shows the velocity and temperature fields for the three grids at the five hundredth time cycle. Note that the location of the center of the eddy in the vapor is nearly the same for the three grid resolutions. These results are typical in that they indicate that the method, while formally first

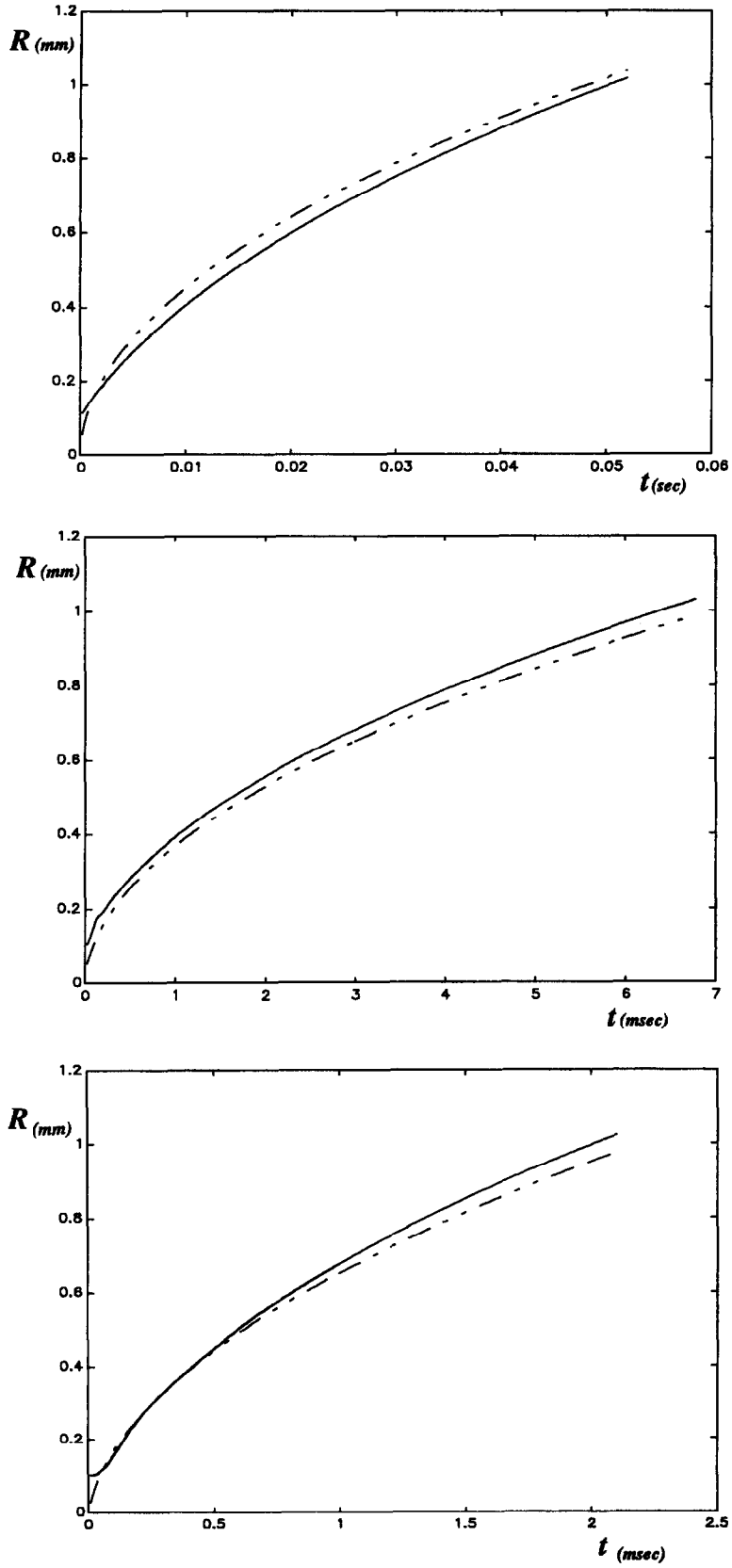

Fig. 4. Comparison of simulated bubble growth curves and analytic solution [2] dashed—analytic, solid—present simulation: Top—$P_0 = 5.0 \times 10^4$ Pa, $\Delta\vartheta = 1.0$, $J = 5.73$; Middle—$P_0 = 1.0 \times 10^5$ Pa, $\Delta\vartheta = 5.0$, $Ja = 15.17$; Bottom—$P_0 = 5.0 \times 10^4$ Pa, $\Delta\vartheta = 5.0$, $Ja = 28.65$.

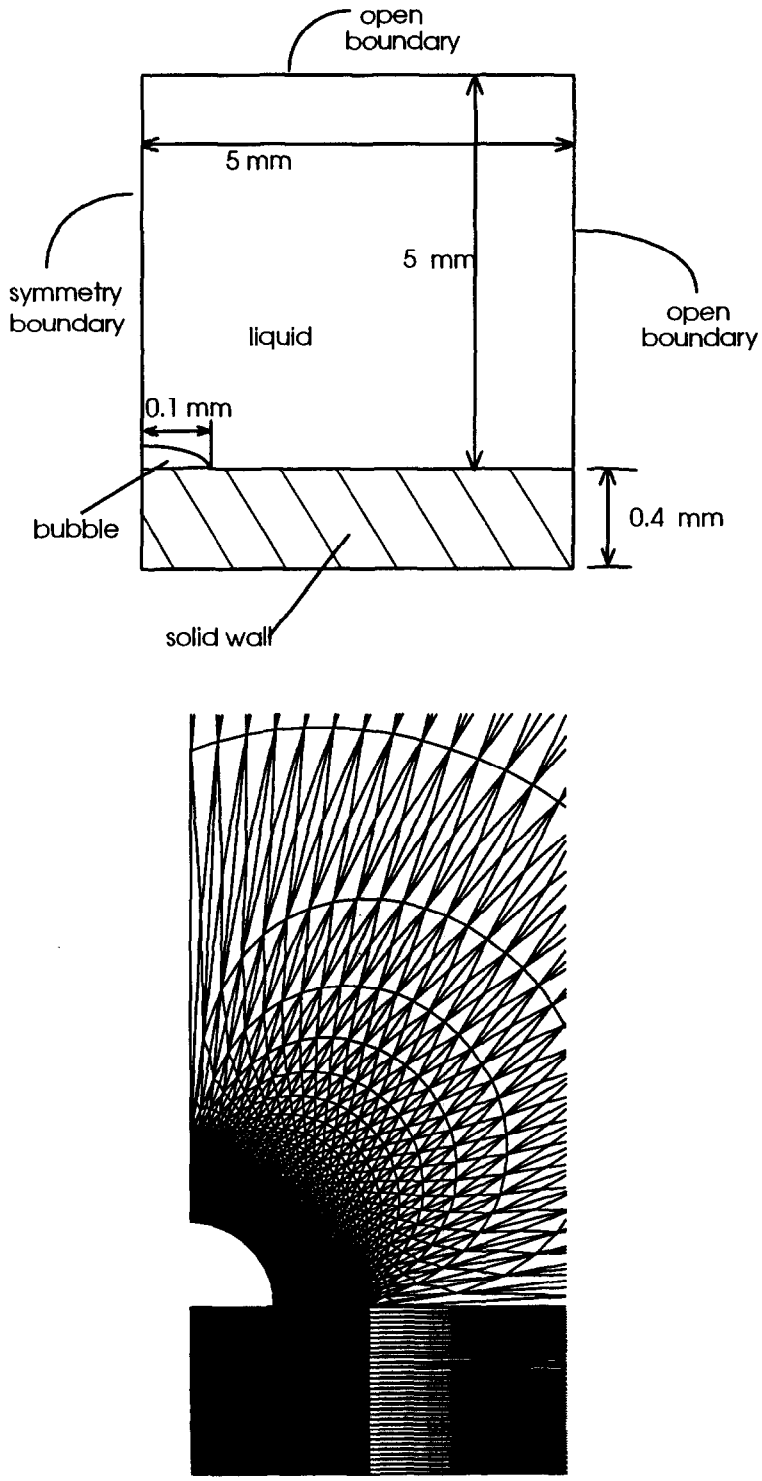

Fig. 5. Computational domain for heterogeneous bubble growth simulations. Computational grid for heterogeneous bubble growth simulations (vapor elements not shown for clarity). 516 vapor nodes, 1201 liquid nodes, 25 interfacial nodes, 3515 solid nodes.

Table 3. Bubble cap location and velocities for three grid resolutions at time cycle 500

	Cap position	Interface velocity	Liquid velocity	Vapor velocity
Coarse grid	0.0001571	0.7032	0.6811	0.6649
Medium grid	0.0001546	0.9132	0.8754	0.7529
Fine grid	0.0001544	0.9712	0.9334	0.7739

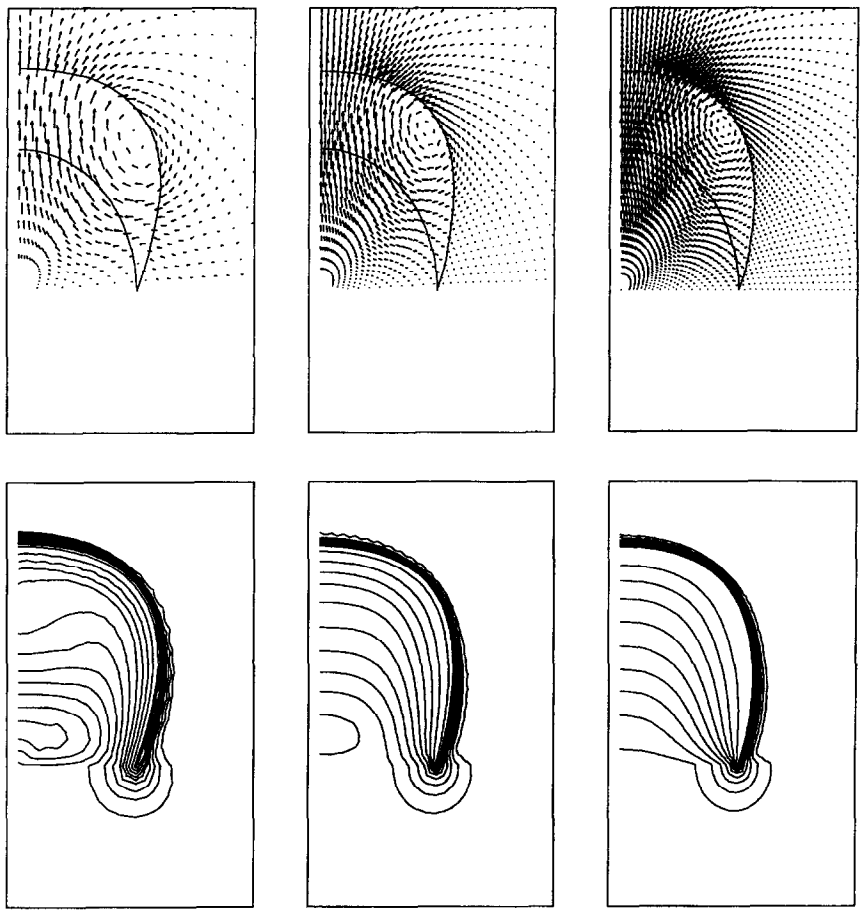

Fig. 6. Velocity field and temperature contours for convergence test. Twenty contours starting at $\vartheta = 372.0$ and incremented by 0.2 K. Upper left and lower left—low grid resolution. Upper middle and lower middle—medium grid resolution. Upper right and lower right—high grid resolution.

order, obtains results more typical of a higher order method. These results do not indicate a converged solution, they do however show that the method is converging. We continue this simulation on the fine grid until the 15 000th time cycle. Figure 7 shows the temperature field at various time cycles. Note that the method is capturing the thermal layer as it moves with the bubble surface and that the thermal field in the solid is providing some of the energy for vaporization.

The level of superheat in the previous simulation was such that the bubble shape remained nearly spherical. In the following simulation we double the liquid superheat. Shown in Fig. 8 is the bubble shape at various time cycles. As the interface propagates outward near the wall there is an apparent microlayer like region forming at the base of the bubble. The grid in the microlayer region has become compressed and distorted and we must stop the simulation near the last time cycle shown in the figure. This simulation indicates a possible mechanism for microlayer formation under low pressure and high superheat conditions as the rapid bubble growth is such that the inertia forces are large enough to produce a non-spherical bubble shape with increased curvature near

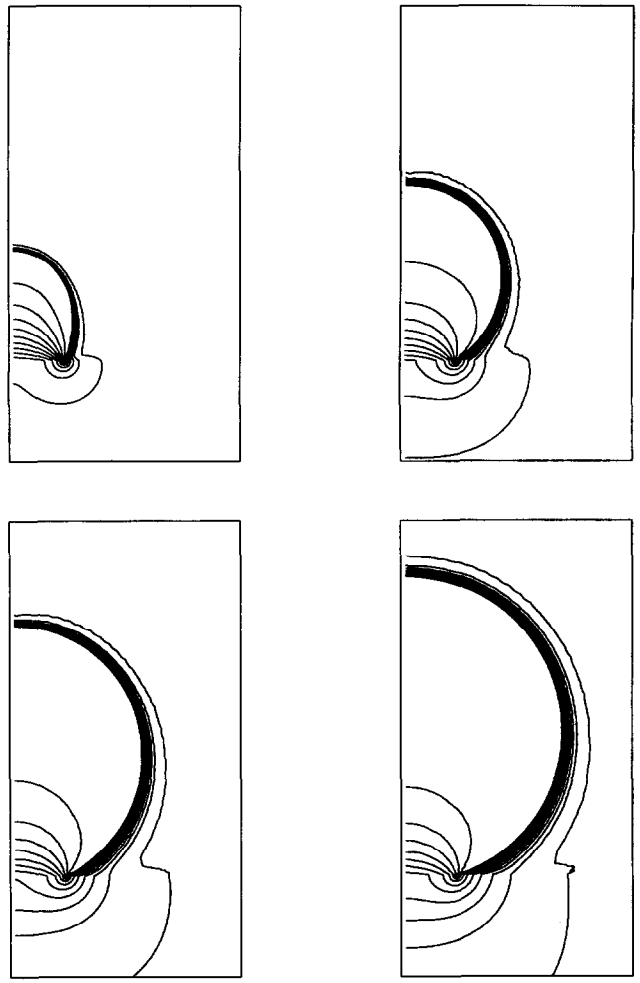

Fig. 7. Temperature contours for depressurization simulation. Twenty contours starting at $\vartheta = 372.0$ and incremented by 0.2 K. Upper left—ncyc = 1000. Upper right—ncyc = 5000. Lower left—ncyc = 10 000. Lower right—ncyc = 15 000.

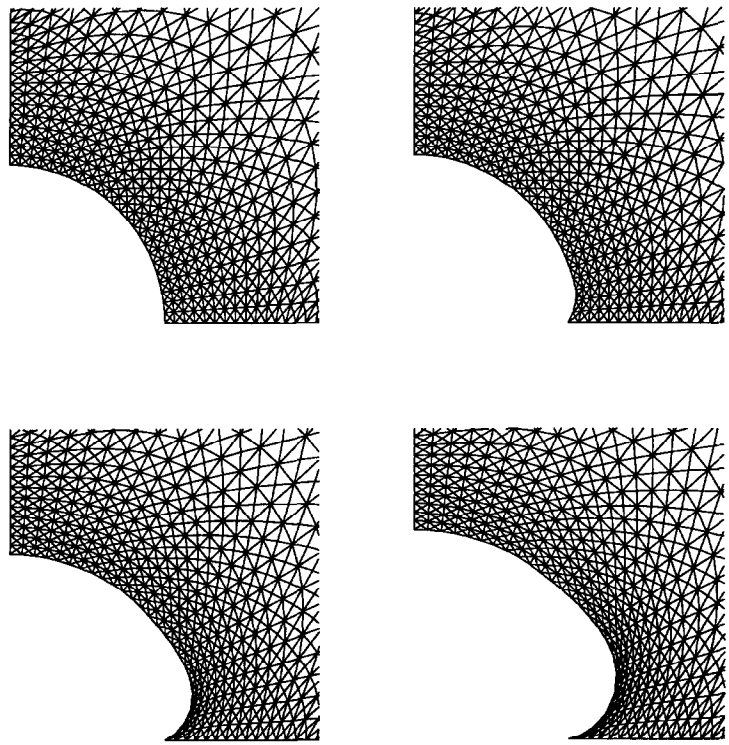

Fig. 8. Bubble shape for final depressurization simulation. Time step is 0.02 μs. Upper left—ncyc = 0. Upper right—ncyc = 500. Lower left—ncyc = 1000. Lower right—ncyc = 1500.

the wall. This simulation, while far from being a complete simulation of microlayer formation, does indicate that our interface tracking method has the potential to be an important tool in the study of heterogeneous bubble growth.

5. CONCLUSIONS

We have presented a numerical method suitable for the local simulation of axisymmetric two-phase flows with mass transfer. Calculation of these flows is complicated by a moving phase interface across which the normal component of velocity and the pressure are discontinuous. These calculations are further complicated by the presence of steep temperature profiles near the moving phase interface. Our method addresses these difficulties by tracking the phase interface and by moving the computational grid in such a way as to keep a high grid resolution near the interface. We feel that this approach may eventually facilitate a deeper understanding of nucleate bubble growth as the hydrodynamics and the bubble shape can be obtained as part of the solution.

Acknowledgments—This work was supported in part by the Idaho National Engineering Laboratories Long Term Research Initiative in Computational Mechanics. The author would also like to thank Prof. John A. Trapp at the University of Colorado at Denver for the many insightful discussions during the period of this work. The author extends additional thanks to Youcef Saad for making the iteration package SPARSKIT2 available.

REFERENCES

1. Plesset, M. S. and Zwick, S. A., The growth of vapor bubbles in superheated liquids. *Journal of Applied Physics*, 1954, **25**(4), 493.
2. Mikic, B. B., Rohsenow, W. M. and Griffith, P. On bubble growth rates. *International Journal of Heat and Mass Transfer*, 1970, **13**, 657–666.
3. Cooper, M. G. and Lloyd, A. J. P., The microlayer in nucleate pool boiling. *International Journal of Heat and Mass Transfer*, 1969, **12**, 895–913.
4. Koffman, L. D. and Plesset, M. S., Experimental observations of the microlayer in vapor bubble growth on a heated solid. *Journal of Heat Transfer*, 1983, **105**, 625–632.
5. Wang, Z. and Bankoff, S. G., Bubble growth on a solid wall in a rapidly-depressurizing liquid pool. *International Journal of Multiphase Flow*, 1991, **17**(4), 425–427.
6. Mei, R., Chen, W. and Klausner, J. F., Vapor bubble growth in heterogeneous boiling—I. Formulation. *International Journal of Heat and Mass Transfer*, 1995, **38**(5), 909–919.
7. Mei, R., Chen, W. and Klausner, J. F., Vapor bubble growth in heterogeneous boiling—II. Growth rate and thermal fields. *International Journal of Heat and Mass Transfer*, 1995, **38**(5), 921–934.
8. Guo, Z. and El-Genk, M. S., Liquid microlayer evaporation during nucleate boiling on the surface of a flat composite wall. *International Journal of Heat and Mass Transfer*, 1994, **37**(11), 1641–1655.
9. Van Carey, P., *Liquid–Vapor Phase Change Phenomena*. Taylor and Francis, PA, 1992
10. Zeng, L. Z., Klausner, J. F. and Mei, R., A unified model for the prediction of bubble detachment diameters in boiling systems—1. Pool boiling. *International Journal of Heat and Mass Transfer*, 1993, **36**(9), 2261–2270.
11. Lee, R. C. and Nydahl, J. E., Numerical calculation of bubble growth in nucleate boiling from inception through departure. *Journal of Heat Transfer*, 1989, **111**, 474–479.
12. Patil, R. K. and Prusa, J., Numerical solutions for asymptotic, diffusion controlled growth of a hemispherical bubble on an isothermally heated surface. *HDT*—170, 63–70. *Experimental/Numerical Heat Transfer in Combustion and Phase Change*. ASME, 1991.
13. Hirt, C. W. and Nichols, B. D., Volume of Fluid (VOF) method for the dynamics of free boundaries. *Journal of Computational Physics*, 1981, **39**, 201–225.
14. Unverdi, S. O. and Tryggvason, G., A front tracking method for viscous, incompressible, multi-fluid flows. *Journal of Computational Physics*, 1992, **100**, 25–37.
15. Osher, S. and Sethian, J. A., Fronts propagating with curvature dependent speed. Algorithms based on Hamilton–Jacobi. *Journal of Computational Physics*, 1988, **79**, 12–49.
16. Moe, R. and Bendiksen, K. H., Transient simulation of 2-D and 3-D stratified and intermittent two-phase flows. Part I: theory. *International Journal for Numerical Methods in Fluids*, 1993, **16**, 461–487.
17. Ramshaw, J. D. and Trapp, J. A., A numerical technique for low-speed homogeneous two-phase flow with sharp. *Journal of Computational Physics*, 1976, **21**, 438–453.
18. Welch, S. W. J., Local simulation of two-phase flows including interface tracking with mass transfer. *Journal of Computational Physics*, 1995, **121**, 142–154.
19. Delhaye, J. M., Jump conditions and entropy sources in two-phase systems. Local instant formulation. *International Journal of Multiphase Flow*, **1**, 395–409.
20. Ishii, M., *Thermo-Fluid Dynamic Theory of Two-Phase Flow*. Eyrolles, 1975.
21. Dell'Isola, F. and Romano, A., A phenomenological approach to phase transition in classical field theory. *International Journal of Engineering Science*, 1987, **25**(11-12), 1469–1475.
22. Huang, A. and Joseph, D. D., Stability of liquid–vapor flow down an inclined channel with phase change. *International Journal of Heat and Mass Transfer*, 1993, **36**(3), 663–672.
23. Fruend, R. W., *Siam J. Sci. Stat. Comp.*, 1993, **14**, 470–482.